Article

Hydrothermal Synthesis of β-Nb$_2$ZnO$_6$ Nanoparticles for Photocatalytic Degradation of Methyl Orange and Cytotoxicity Study

Sarah Ameen Almofty [1],*, Muhammad Nawaz [2],*, Faiza Qureshi [2,3] and Rayanah Al-Mutairi [2]

[1] Department of Stem Cell Research, Institute for Research and Medical Consultations (IRMC), Imam Abdulrahman Bin Faisal University, P.O. Box 1982, Dammam 31441, Saudi Arabia

[2] Department of Nano-Medicine Research, Institute for Research and Medical Consultations (IRMC), Imam Abdulrahman Bin Faisal University, P.O. Box 1982, Dammam 31441, Saudi Arabia; frqureshi@iau.edu.sa (F.Q.); 2220500130@iau.edu.sa (R.A.-M.)

[3] Deanship of Scientific Research, Imam Abdulrahman Bin Faisal University, P.O. Box 1982, Dammam 31441, Saudi Arabia

* Correspondence: saalmofty@iau.edu.sa (S.A.A.); mnnmuhammad@iau.edu.sa (M.N.)

Abstract: β-Nb$_2$ZnO$_6$ nanoparticles were synthesized by a hydrothermal process and calcined at two temperatures, 500 °C and 700 °C, and assigned as **A** and **B,** respectively. X-ray diffraction, together with transmission electron microscopy, revealed that the β-Nb$_2$ZnO$_6$ nanoparticles calcined at 700 °C (**B**) were more crystalline than the β-Nb$_2$ZnO$_6$ calcined at 500 °C (**A**) with both types of nanoparticles having an average size of approximately 100 nm. The physiochemical, photocatalytic, and cytotoxic activities of both types of β-Nb$_2$ZnO$_6$ nanoparticles (**A** and **B**) were examined. Interestingly, the photodegradation of methyl orange, used as a standard for environmental pollutants, was faster in the presence of the β-Nb$_2$ZnO$_6$ nanoparticles calcined at 500 °C (**A**) than in the presence of those calcined at 700 °C (**B**). Moreover, the cytotoxicity was evaluated against different types of cancer cells and the results indicated that both types of β-Nb$_2$ZnO$_6$ nanoparticles (**A** and **B**) exhibited high cytotoxicity against MCF-7 and HCT116 cells but low cytotoxicity against HeLa cells after 24 and 48 h of treatment. Overall, both products expressed similar EC$_{50}$ values on tested cell lines and high cytotoxicity after 72 h of treatment. As a photocatalyst, β-Nb$_2$ZnO$_6$ nanoparticles (**A**) could be utilized in different applications including the purification of the environment and water from specific pollutants. Further biological studies are required to determine the other potential impacts of utilizing β-Nb$_2$ZnO$_6$ nanoparticles in the biomedical application field.

Keywords: β-Nb$_2$ZnO$_6$; photocatalysis; cytotoxicity; zeta potential; methyl orange; hydrothermal

1. Introduction

Nanotechnology has inspired the design of diverse nanoscale materials to fulfill the growing material requirements for environmental, biological, and medical applications [1–6]. Environmental pollution has become a serious global concern due to the rapid increase in population and industries. Most industrial wastes contain high concentrations of toxic substances that accumulate and negatively affect living creatures and the environment [7–10]. Therefore, designing nano-photocatalysts is needed to develop stable and effective photocatalysts for different types of organic pollutants. Recently, semiconductor photocatalysts have been extensively used for the purification of organic pollutants in water. TiO$_2$, for example, is used as a catalyst for the photodegradation of organic pollutants, but with customized application only as it has a wide band gap, poor catalyst recovery, and a tendency to agglomerate [11,12]. Previously, we reported the catalytic degradation of volatile chlorinated compounds by heterostructured nanoparticles which showed enhanced catalytic activity [8,13–18]. Nanomaterials have also been used in the field of medicine and

biology to significantly improve traditional diagnostic and therapeutic techniques [19–22]. They are also used as a powerful tool for the exploration and understanding of physiological processes [23–26] and offer many advantages as they have unique physiochemical attributes, including a large surface area compared to bulk biomolecules, and a stable shape and size which makes them interesting. Nanomaterials are typically smaller than host cells and can enter the host cells easily by cellular endocytosis or cell membrane penetration [27]. Several nanomaterials, such as titanium oxide, silica oxide, gold, copper oxide, copper sulfide, zinc sulfide/bismuth sulfide carbon nanotubes, silver oxide, and carbon-based materials, have been reported for their efficiency in biomedical and photocatalytic applications [28–31]. Interestingly, the composition of zinc incorporated niobium oxide exhibited antibacterial potential against *Staphylococcus aureus* and *Escherichia coli* bacteria [32], suggesting that this composition might have other potential activities yet to be investigated. Zinc oxide is considered an important semiconductor due to its stability, low cost, and excellent electron mobility, but its practical use in photocatalysis is limited due to its wide band gap (3.3 eV) and rapidly recombining electron-hole pairs [29,33]. Several methods have been employed to reduce the band gap such as metal/element doping, heterostructure engineering/construction, and controlling the morphology. Utilizing these strategies, some zinc oxide-based materials such as BioI/ZnO [34], $ZnO@SiO_2$ [35], ZnO/CdSe [36], Ag/ZnO@C [37], and Ag_3PO_4/ZnO [38] have been synthesized successfully for efficient photocatalysis application.

Herein, we report the synthesis of β-Nb_2ZnO_6 nanoparticles (calcined at two different temperatures, 500 °C and 700 °C, designated as **A** and **B**, respectively, to reduce the recombination rate for electron-hole pairs and enhance the nanoparticles' photocatalytic activities [29,39]. The prepared β-Nb_2ZnO_6 nanoparticles were distinguished by X-ray diffraction (XRD), transmission electron microscopy (TEM), BET surface analysis, zeta potential measurement, and diffuse reflectance- spectroscopy. The present work is designed to study (1) the potential photocatalytic activity of β-Nb_2ZnO_6 (**A**) and (**B**) nanoparticles by evaluating the photocatalytic degradation of methyl orange and (2) to determine the cytotoxicity of β-Nb_2ZnO_6 nanoparticles by measuring the cell viability of treated cancer cells to obtain the EC_{50} values.

2. Results and Discussion

2.1. Characterization of β-$ZnNb_2O_6$ Nanoparticles

The morphology of the β-Nb_2ZnO_6 (**A**) and (**B**) nanoparticles was determined by TEM. Figure 1a,b displays representative images of β-Nb_2ZnO_6 nanoparticles (**A** and **B**) calcined at 500 °C (**A**) and 700 °C (**B**), respectively. The average size of the β-Nb_2ZnO_6 (**A**) and (**B**) nanoparticles was 100 nm with nanoplate-like morphology. XRD was employed to find out the crystal structure of the β-Nb_2ZnO_6 (**A**) and (**B**) nanoparticles. Figure 1c shows the XRD configuration of β-Nb_2ZnO_6 calcined at 500 °C (**A**) and 700 °C (**B**). The results indicate that β-Nb_2ZnO_6 nanoparticles calcined at 700 °C (**B**) have more crystalline features than β-Nb_2ZnO_6 calcined at 500 °C (**A**). This further suggested that crystallinity can be achieved by calcining the sample at a high temperature. The peaks are well-matched with ICDD card no. 00-028-1477 with an unknown crystal system.
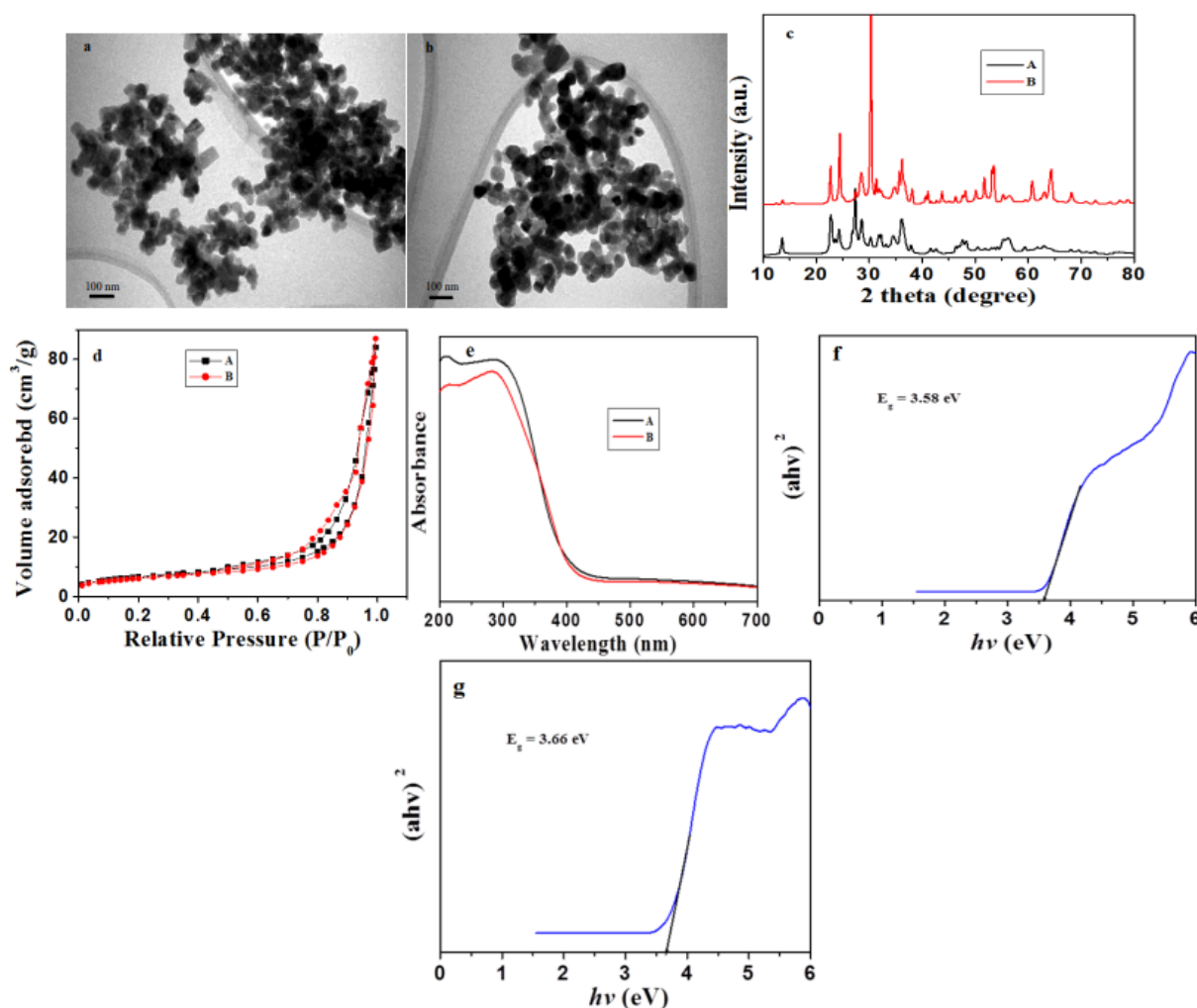
Figure 1. Physical characterization of the β-Nb$_2$ZnO$_6$ nanoparticles. TEM images of β-Nb$_2$ZnO$_6$ nanoparticles calcined at 500 °C (**A**) and 700 °C (**B**) (**a,b**), XRD pattern of β-Nb$_2$ZnO$_6$ (**A** and **B**) (**c**), N2 adsorption-desorption isotherm of β-Nb$_2$ZnO$_6$ (**A** and **B**) (**d**), UV-Vis spectra of β-Nb$_2$ZnO$_6$ (**A** and **B**) (**e**), Tauc plots of β-Nb$_2$ZnO$_6$ (**A** and **B**) (**f,g**).

N$_2$-adsorption-desorption isotherm examination was completed to review the pore size and surface area of the β-Nb$_2$ZnO$_6$ nanoparticles. Figure 1d shows the N$_2$ sorption isotherms and porosity of the β-Nb$_2$ZnO$_6$ nanoparticles. The typical type-IV isotherm with a narrow H3-type hysteresis loop in Figure 1e suggested that the particles were mesoporous [40]. The BET surface area of β-Nb$_2$ZnO$_6$ calcined at 500 °C (**A**) was calculated to be 22.67 m^2/g (pore size: 18.95 nm; pore volume 0.130 cm^3/g), while the sample calcined at 700 °C (**B**)was found to have a surface area of 20.81 m^2/g (pore size: 19.06 nm; pore volume 0.135 cm^3/g). The slightly smaller surface area of β-Nb$_2$ZnO$_6$ nanoparticles calcined at 700 °C (**B**) is due to the improvement in the crystalline structure of the β-Nb$_2$ZnO$_6$ nanoparticles at high temperature.

Figure 1e displays the UV-visible absorption spectrum of β-Nb$_2$ZnO$_6$ nanoparticles (**A** and **B**) recorded in the range of 200–700 nm. The band gap can be calculated by the Tauc formula:

$$(\alpha\, hv)^{2/n} = A\,(hv - E_g),$$

where α represents absorption coefficient, h the Plank's constant, v the light frequency, A an energy independent proportionality constant characteristic of the material, and E$_g$ the optical band gap. The exponent n defines the nature of the optical transitions. The direct transition band gaps were determined from the Tauc plots of $(\alpha\, hv)^2$ vs. hv, (Figure 1f,g).

The optical band gap E_g values for β-Nb_2ZnO_6 nanoparticles (**A** and **B**) were 3.58 and 3.66 eV, respectively.

The composition of the product was further confirmed by EDX analysis. The represented EDX spectrum and elemental mapping are shown in Figure 2. It is clear from Figure 2 that the product contains Nb, Zn, and O. K and L correspond to the amount of energy possessed by the X-ray emitted by an electron in the K and L shells, respectively.
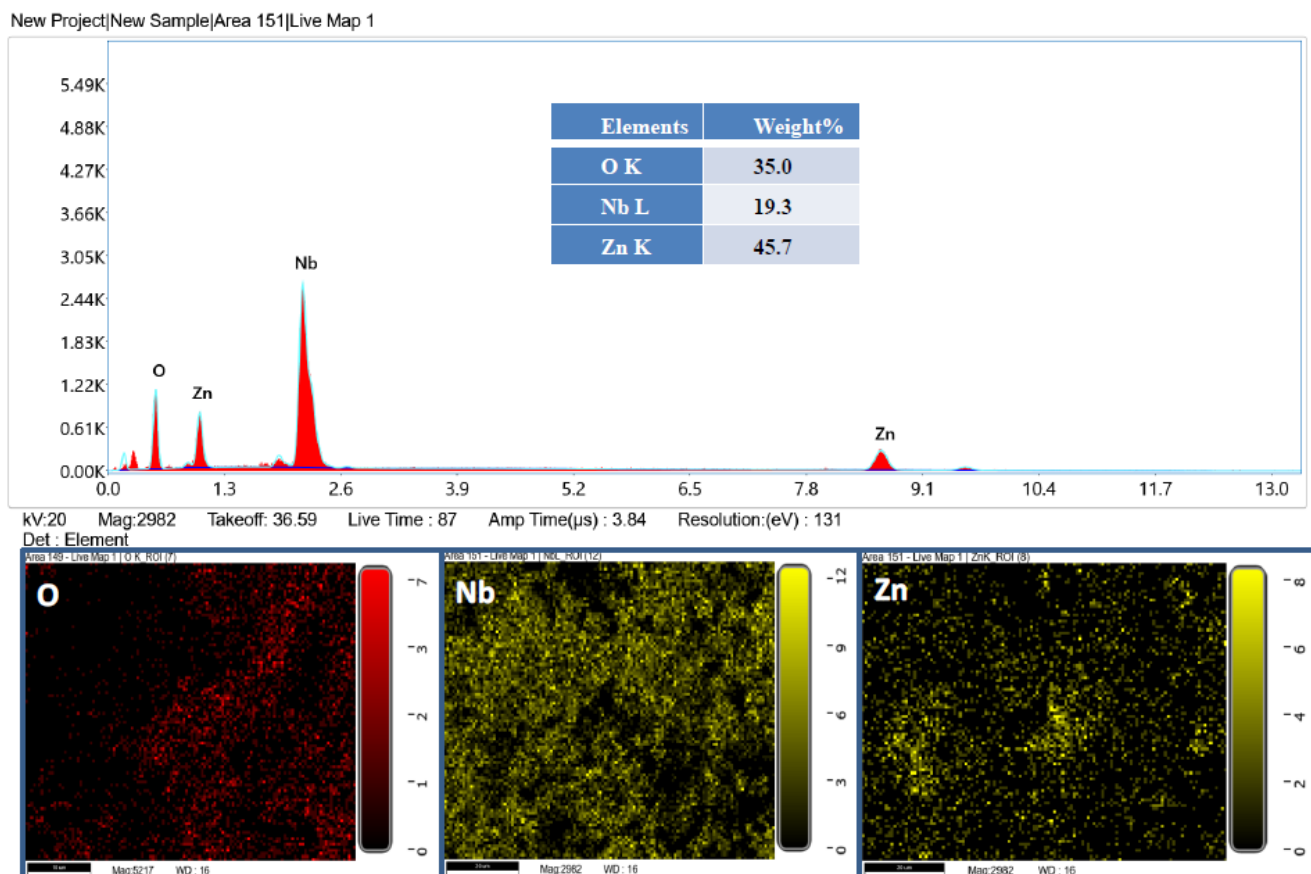

Figure 2. EDX spectrum and EDX mapping of β-Nb_2ZnO_6 nanoparticles (**A**).

Zeta potential is an imperative technique for determining the surface charge and stability of nanoparticles and can tell us the state of nanoparticle surface nature. The zeta potential of β-Nb_2ZnO_6 nanoparticles (**A** and **B**) is shown in Figure 3; both β-Nb_2ZnO_6 nanoparticles (**A** and **B**) have a less variation in the zeta potential and it was observed at -12.9 and -13 mV, respectively, while the polydispersity index (PDI) of β-Nb_2ZnO_6 nanoparticles (**B**) (PDI: 0.518) was slightly decreased as compared to β-Nb_2ZnO_6 nanoparticles (**A**) (PDI: 0.690). Similarly, the particle size distribution of β-Nb_2ZnO_6 nanoparticles (**A** and **B**) was observed at 517 and 453 nm, respectively. Results indicated almost similar stability of β-Nb_2ZnO_6 nanoparticles (**A** and **B**) in the deionized water.
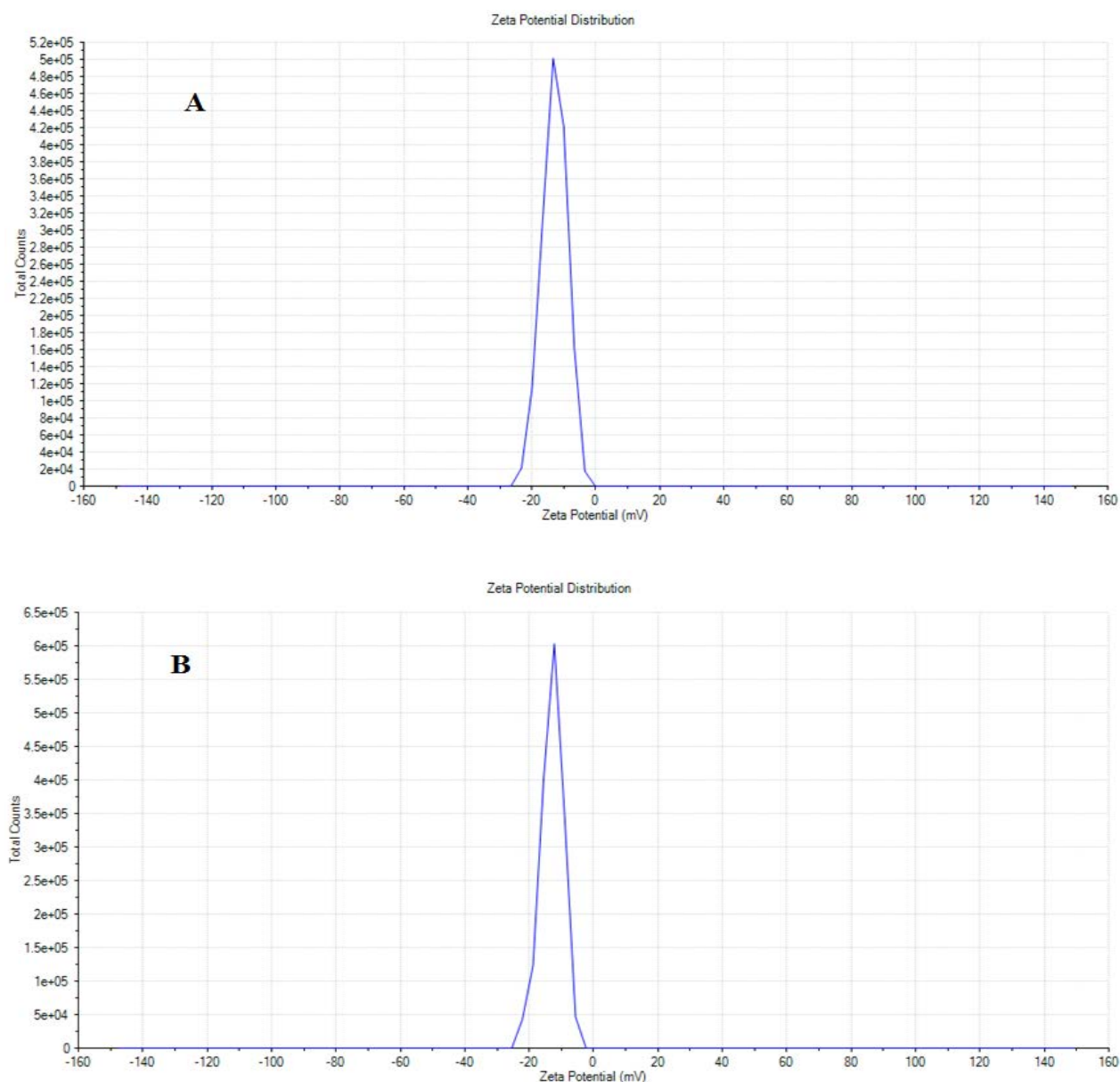
Figure 3. Zeta potential of β-Nb$_2$ZnO$_6$ nanoparticles (**A** and **B**).

2.2. Photocatalytic Activity of β-Nb$_2$ZnO$_6$ Nanoparticles

The photodegradation potential of β-Nb$_2$ZnO$_6$ nanoparticles (**A** and **B**) was tested using methyl orange as a typical environmental pollutant under UV-Vis light irradiation. As evident in Figure 4a, the absorption peak at 465 nm, which indicated the presence of methyl orange, decreased in the presence of β-Nb$_2$ZnO$_6$ nanoparticles (**A**) with increased reaction time. However, for sample B, the decrease in the absorption peak at 465 nm was small, even after long reaction times (Figure 4b). The photodegradation of methyl orange proceeded faster with β-Nb$_2$ZnO$_6$ nanoparticles calcined at 500 °C (**A**) (Figure 4c) compared to β-Nb$_2$ZnO$_6$ nanoparticles calcined at 700 °C (**B**). The photocatalytic degradation of methyl orange without β-Nb$_2$ZnO$_6$ nanoparticles was also studied; these results indicated that there was no degradation of methyl orange without β-Nb$_2$ZnO$_6$ nanoparticles, demonstrating that photocatalytic degradation of methyl orange can be achieved with β-Nb$_2$ZnO$_6$ nanoparticles (**A**) (Figure 4c). The photocatalytic efficiency of β-Nb$_2$ZnO$_6$ nanoparticles (**A**) was higher as compared to MO and β-Nb$_2$ZnO$_6$ nanoparticles (**B**) (Figure 4d). The high photocatalytic activity of the β-Nb$_2$ZnO$_6$ nanoparticles (**A**) could be credited to the highly

effective separation of carrier charges as well as the slowed recombination of electron-hole pairs during the photocatalysis process causing high photocatalytic activity [41,42]. It has been noticed that various constraints such as pore dimension and formation and surface features and crystallinity affect the photocatalytic ability. The lesser photocatalytic ability of sample B may be caused by a decline in surface area, destruction of pores at high temperature, crystal growth, and shielding of active sites on the surface of sample B. This may result in a decrease in surface-active sites on the surface and a reduction in charge separation/transfer, which in turn causes low photocatalytic activity [40]. Furthermore, the kinetics of methyl orange degradation was evaluated to establish the rate constants and was found to follow pseudo-first order reactions:

$$\ln(C_0/C) = k\,t$$

where C_0 and C are the initial and the time-dependent concentrations of methyl orange, t is the time (minutes) and k is the rate constant (min^{-1}). As it is clear from Figure 4e), β-Nb_2ZnO_6 nanoparticles (A) revealed a high rate constant (0.0351 min^{-1}) in the degradation of methyl orange as compared to β-Nb_2ZnO_6 nanoparticles (B) and blank methyl orange.
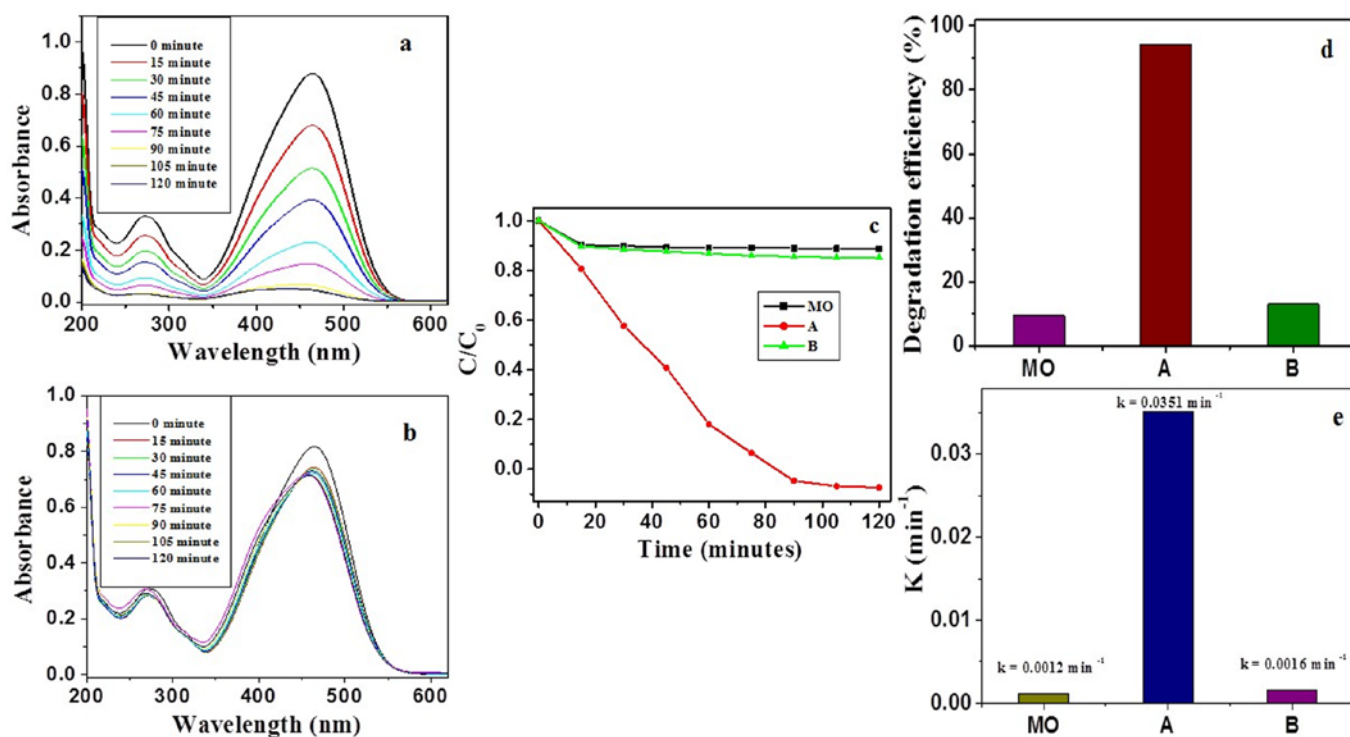

Figure 4. Changes in the UV-Vis absorption spectrum of methyl orange with 50 mg β-Nb_2ZnO_6 (**A** and **B**) after different irradiation times (**a**,**b**), photocatalytic activities of β-Nb_2ZnO_6 nanoparticles (**A** and **B**) for methyl orange degradation over 120 min (**c**), degradation efficiency of β-Nb_2ZnO_6 nanoparticles (**A** and **B**) (**d**) comparison of rate constants (**e**).

Photocatalysis experiments were further conducted to understand the role of reactive species during the photocatalysis process. Scavenging agents such as isopropanol, *p*-benzoquinone, and ethylenediaminetetraacetic acid (EDTA) in the presence of β-Nb_2ZnO_6 nanoparticles (**A**) were used applying the same reaction conditions (Figure 5a). It was perceived that when EDTA was introduced in the reaction, there was a slight decline in the photocatalytic activity, suggesting the limiting role of the hole (h^+) in photocatalysis. Additionally, when *p*-benzoquinone was used in the reaction, there was more decline in the photocatalytic activity, indicating that reactive superoxide radical ($\bullet O_2^-$) performs an important role in photocatalysis process. Similarly, an isopropanol addition in the reaction

resulted in a further decline in the photocatalytic activity, signifying that hydroxyl (●OH) plays a significant role in the photocatalytic degradation of methyl orange [43].
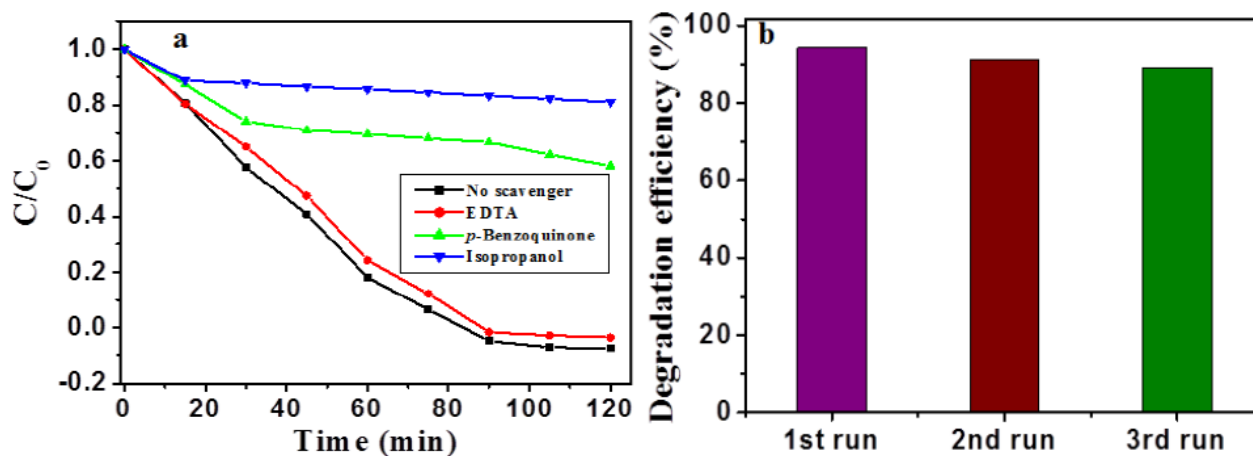

Figure 5. Degradation profile of methyl orange in the presence of scavengers (**a**); reusability of β-Nb_2ZnO_6 nanoparticles (**A**) after 3 runs (**b**).

The recycling/reusability of a photocatalyst is important in the photocatalysis process, so we have tested the stability of β-Nb_2ZnO_6 nanoparticles (**A**) by recycling experiments. The same experimental conditions were used as in the photocatalytic experiment, except that after each run β-Nb_2ZnO_6 was separated, and fresh methyl orange was used. We performed three recycling experiments to check the stability of the β-Nb_2ZnO_6 nanoparticles (**A**). As it is clear from Figure 5b, the differences in photocatalytic activity after each recycling were minor, indicating the stability of β-Nb_2ZnO_6 nanoparticles.

The mechanism of charge transfer on β-Nb_2ZnO_6 nanoparticles is illustrated in Figure 6, that is, the generation of electron-hole pairs (e^-/h^+), under UV light irradiation, in the conduction and valence bands of β-Nb_2ZnO_6 nanoparticles, respectively. The electrons in the conduction band of β-Nb_2ZnO_6 nanoparticles reduce the molecular oxygen to ●O_2^- and holes on the valence band interact with ^-OH to produce ●OH radicals, triggering the reduction and degradation of methyl orange [18].
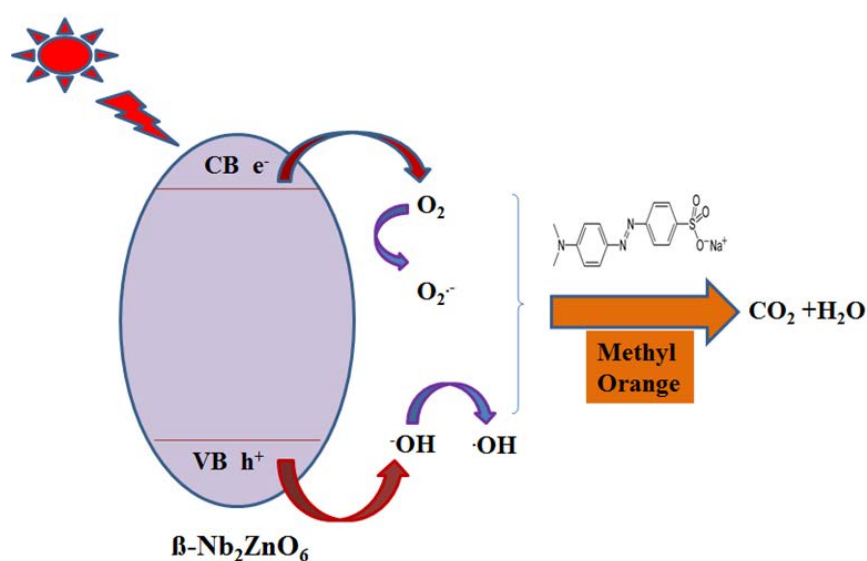

Figure 6. Schematic illustration of photocatalytic activity of β-Nb_2ZnO_6 for the degradation of methyl orange.

2.3. Cytotoxicity of β-Nb$_2$ZnO$_6$ Nanoparticles

The cytotoxicity of β-Nb$_2$ZnO$_6$ nanoparticles had been recorded by estimating the cell viability via MTT assay [17,18]. MCF-7, HCT116, and HeLa cells were treated with pre-determined concentrations (1, 0.5, 0.25, and 0.125 mg/mL) of β-Nb$_2$ZnO$_6$ nanoparticles (**A**) and (**B**) for 24, 48, and 72h, followed by the cells incubating in an MTT solution, which utilizes a formazan, colorimetric reduction of tetrazolium salt (3-(4,5-dimethylthiazol-2-yl)-2,5-diphenyltetrazolium bromide) by living cells, producing purple crystals which, after dissolving in DMSO, were assayed at 570 nm on Elisa microplate reader.

The assay exposed the increased cytotoxic potential of nanoparticles A at 0.5 and 1 mg/mL against MCF-7 and HCT116 cells with 30–47% cell viability and over 50% cell viability at the reduced nanoparticle concentrations following 24 and 48 h of treatment (Figure 7a,b). The cell viability of HeLa cells with nanoparticles (**A**) and (**B**) displayed less disparity among the used concentrations with the average cell viability being over 50% after 24 and 48 h of treatment. Interestingly, (**A**) and (**B**) exhibited increased cytotoxic action towards MCF-7, HCT116, and HeLa cells after 72 h of treatment at 0.250 mg/mL (Figures 7c and 8c). However, the concentration effective for half-maximal response (EC$_{50}$) values were estimated for (**A**) and (**B**) nanoparticles in each cell line after obtaining the average of cell viability% taken from the tested time points as EC$_{50}$ = 0.401 mg/mL (**A**) and 0.305 mg/mL (**B**) for MCF-7 cells, 0.375 mg/mL (**A**) and 0.311 mg/mL (**B**) for HCT116 cells, and 1 mg/mL (**A**) and 1.2 mg/mL (**B**) for HeLa cells (Figure 9). Conclusively, the studies showed high cytotoxic action of β-Nb$_2$ZnO$_6$ nanoparticles (**A**) and (**B**) for MCF-7 and HCT116 cells and low cytotoxic action for HeLa cells, for which there is a need to explore further biomolecular assays to ascertain reasons for variable cytotoxicity. The present data, however, confirms that β-Nb$_2$ZnO$_6$ (**A**) and (**B**) have a close cytotoxic activity and further optimization is required for the enhancement of biocompatibility of β-Nb$_2$ZnO$_6$ for large-scale utilization.
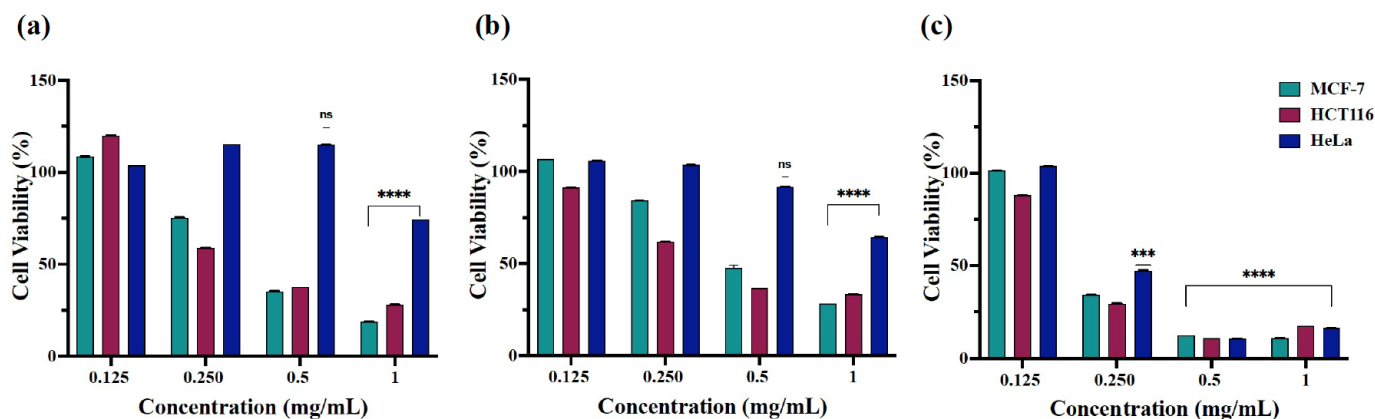

Figure 7. Cell viability (%) of MCF-7, HCT116 and HeLa cells treated with β-Nb$_2$ZnO$_6$ nanoparticles (**A**). The graph shows the cytotoxic effect of β-Nb$_2$ZnO$_6$ nanoparticles (**A**) as highly significant (****) when compared with untreated (control) cells, (**a**) treatment for 24 h, (**b**) 48 h and (**c**) 72 h. *P* value is set at <0.05 (* if $P \leq 0.05$, ** if $P \leq 0.01$, *** if $P \leq 0.001$, **** if $P \leq 0.0001$).
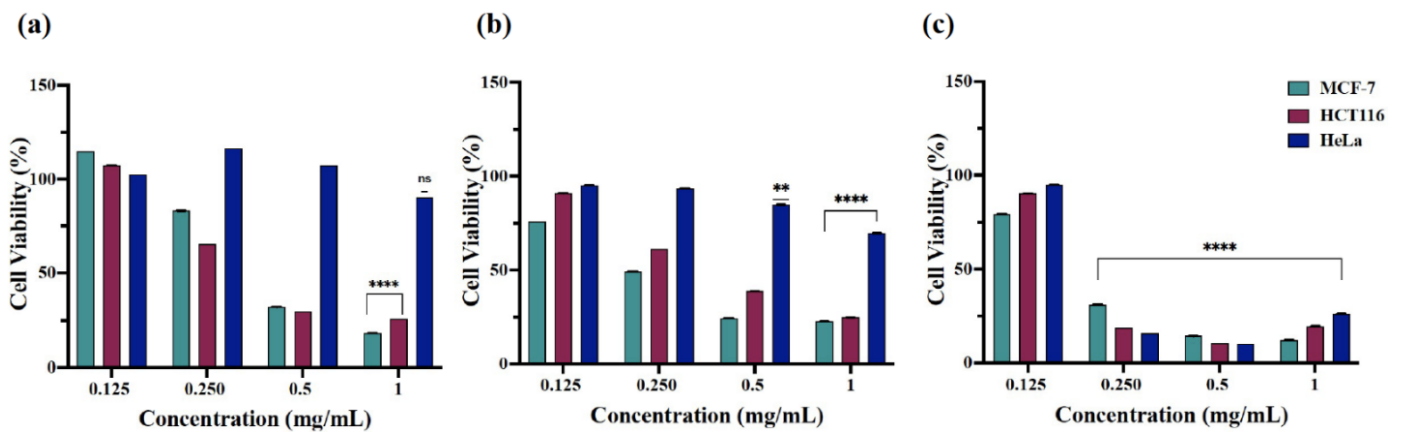
Figure 8. Cell viability (%) of MCF-7, HCT116 and HeLa cells treated with β-Nb$_2$ZnO$_6$ nanoparticles (**B**). The graph shows the cytotoxic effect of β-Nb$_2$ZnO$_6$ (**B**) nanoparticles as highly significant (****) when compared with untreated (control) cells, (**a**) treatment for 24 h, (**b**) 48 h and (**c**) 72 h. P value is set at <0.05 (* if $P \leq 0.05$, ** if $P \leq 0.01$, *** if $P \leq 0.001$, **** if $P \leq 0.0001$).
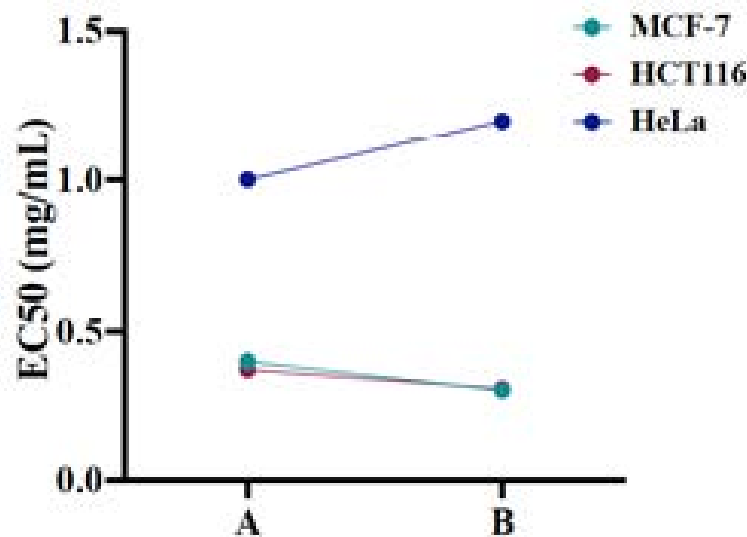

Figure 9. EC$_{50}$ values of β-Nb$_2$ZnO$_6$ nanoparticles (**A**) and (**B**). Half maximal effective concentration (EC$_{50}$) of β-Nb$_2$ZnO$_6$ (**A**) and (**B**) nanoparticles were determined for each cell line.

2.4. Imaging of Nb$_2$ZnO$_6$ Nanoparticles Treated Cells

The morphological impacts of β-Nb$_2$ZnO$_6$ nanoparticles (**A** and **B**) on treated cells were indicated by imaging using confocal microscopy. MCF-7, HCT116, and HeLa cells together with 0.25, 0.5, and 1 mg/mL of β-Nb$_2$ZnO$_6$ (**A**) and (**B**) nanoparticles were treated for 48 h and fixed with cold absolute methanol prior to the staining procedure. The cells were stained with DAPI, a blue fluorescent dye that binds to adenine/thymine-rich segments on DNA (blue) to visualize the nuclei. Treated MCF-7, HCT116, and HeLa cells showed nuclear fragmented structures at the lowest used concentration as well as a reduction in cell number in comparison to the untreated cells. It was obvious that β-Nb$_2$ZnO$_6$ (**A**) and (**B**) were dramatically changing the morphology of treated cells upon increasing the concentration, as shown in Figure 10. Interestingly, β-Nb$_2$ZnO$_6$ (**A**) and (**B**) treated HeLa cells showed more DAPI stained cells which is consistent with the cell viability results and estimation EC$_{50}$ that HeLa cells were weakly affected by the used concentrations after 48 h of treatment (Figures 10 and 11). The imaging results clearly demonstrated a correlation with the cytotoxicity results of β-Nb$_2$ZnO$_6$ nanoparticles, implicating their

ability in inducing morphological changes and nuclear fragmentation which might be associated with a cell death mechanism.
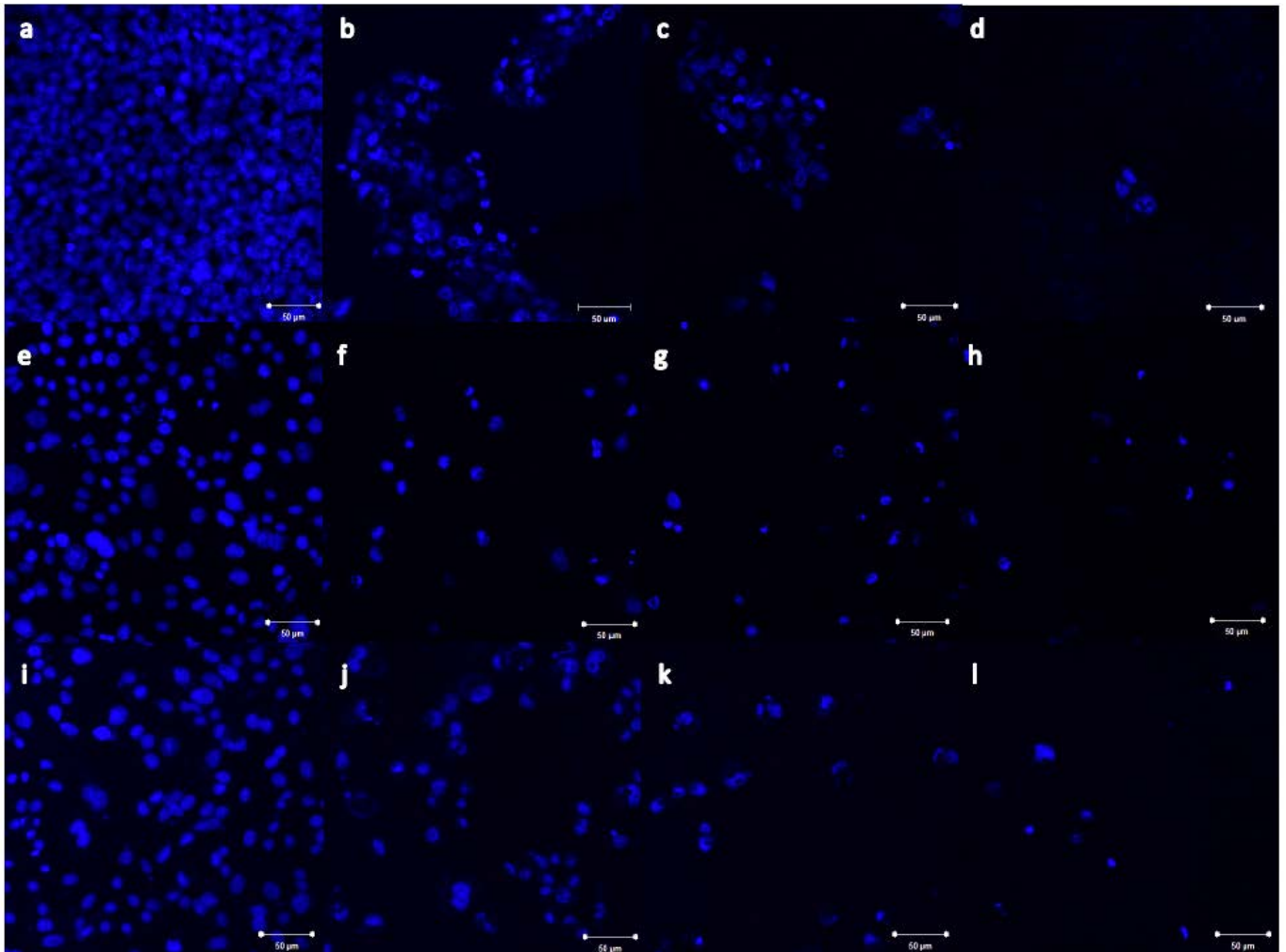

Figure 10. Confocal microscopic images of MCF-7, HCT116 and HeLa cells treated with β-Nb_2ZnO_6 nanoparticles (**A**). The cells were treated for 48 h with 0.25, 0.5, and 1 mg/mL of β-Nb_2ZnO_6 (**A**) nanoparticles. (**a**) Untreated MCF-7 cells, (**b–d**) MCF-7 cells treated with 0.25, 0.5 and 1 mg/mL of β-Nb_2ZnO_6 (**A**), respectively. (**e**) Untreated HCT116 cell, (**f–h**) HCT116 cells treated with 0.25, 0.5 and 1 mg/mL of β-Nb_2ZnO_6 (**A**), respectively. (**i**) Untreated HeLa cells, (**j–l**) HeLa cells treated with 0.25, 0.5 and 1 mg/mL of β-Nb_2ZnO_6 (**A**), respectively. The blue tint signifies DAPI-stained cell nuclei (200× magnification, scale bar is 50 µm for all images).
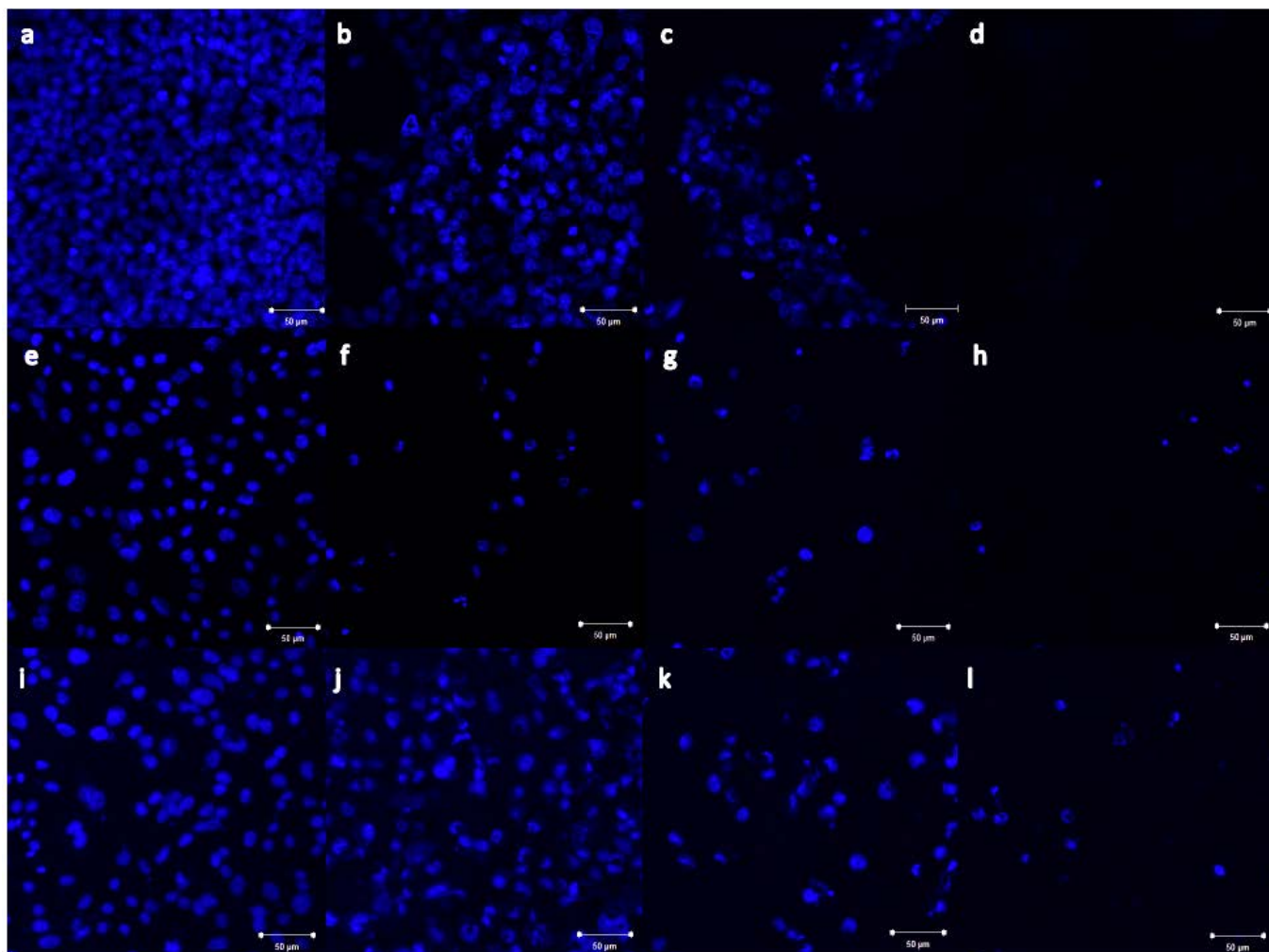
Figure 11. Confocal microscopic images of MCF-7, HCT116 and HeLa cells cells treated with β-Nb$_2$ZnO$_6$ nanoparticles (**B**). The cells were treated for 48 h with 0.25, 0.5 and 1 mg/mL of β-Nb$_2$ZnO$_6$ (**B**) nanoparticles. (**a**) Untreated MCF-7 cells, (**b–d**) MCF-7 cells treated with 0.25, 0.5 and 1 mg/mL of β-Nb$_2$ZnO$_6$ (**B**), respectively. (**e**) Untreated HCT116 cell, (**f–h**) HCT116 cells treated with 0.25, 0.5 and 1 mg/mL of β-Nb$_2$ZnO$_6$ (**B**), respectively. (**i**) Untreated HeLa cells, (**j–l**) HeLa cells treated with 0.25, 0.5 and 1 mg/mL of β-Nb$_2$ZnO$_6$ (**B**), respectively. The blue tint signifies DAPI-stained cell nuclei (200x magnification, scale bar is 50 μm for all images).

3. Materials and Methods

3.1. Synthesis of β-Nb$_2$ZnO$_6$

Niobium chloride (0.270 g) and zinc nitrate (0.2974 g) were weighed and shifted to a Teflon-lined autoclave with 20 mL of distilled water. After stirring, urea (0.2402 g) and ammonium fluoride (0.148 g) were added to the mixture. After stirring, the autoclave was heated at 200 °C for 12 h. The obtained precipitation was centrifuged and washed repeatedly using deionized water, followed by washing with ethanol, and dried overnight (60 °C). The samples were calcined at 500 °C and 700 °C in the furnace and assigned as (**A**) and (**B**), respectively.

The morphology and size of β-Nb$_2$ZnO$_6$ nanoparticles (**A**) and (**B**) were determined by a transmission electron microscope (TEM) (FEI, Morgagni 268, Brno, Czech Republic) and X-ray diffraction (Rigaku, Japan) quantified with Cu-Kα radiation (λ = 1.5418 Å) with a 1° per minute speed of scanning (range 10–80°). Surface area (BET) was determined by Micromeritics ASAP 2020 PLUS (Norcross, GA, USA) by degassing the samples (180 °C) and by employing N$_2$ adsorption data with a range of relative pressure (P/P$_0$) from 0.0

to 1.0. A diffuse reflectance UV-visible spectrophotometer was used for recording the UV-Visible spectra (UV-Vis, JASCO V-750, Great Dunmow, Essex, UK).

3.2. Photocatalytic Activity

The aim of evaluating the photocatalytic action of the β-Nb_2ZnO_6 nanoparticles (**A**) and (**B**) was realized by achieving photodegradation of methyl orange under visible light irradiation using a Xenon lamp (300 W, with > 400 nm cut-off filter). Each experimental set consisted of 0.050 g of β-Nb_2ZnO_6 nanoparticles (**A**) and (**B**) dispersed in 50 mL methyl orange (aqueous 10 mg/L). For the establishment of an adsorption-desorption balance between the photocatalyst and methyl orange, the solution was continuously stirred for a specific period in the dark followed by illumination with the Xenon lamp. After 15 min, 3 mL of the sample was removed and centrifuged. The degradation of methyl orange was calculated at 465 nm using UV-Visible spectrophotometry. The extent of degradation was calculated by

$$\text{Efficiency (\%)} = (C_0 - C)/C_0 \times 100$$

where C_0 is the initial methyl orange concentration and C is the time-dependent concentration of methyl orange following irradiation with β-Nb_2ZnO_6 nanoparticles (**A** and **B**).

3.3. Cell Culture and Cytotoxicity of β-Nb_2ZnO_6 Nanoparticles

The human cell lines (American Type Culture Collection, Manassas, VA, USA) applied to test the cytotoxicity of β-Nb_2ZnO_6 nanoparticles (**A** and **B**) against were: MCF-7 (breast cancer), HCT116 (human colon cancer), and HeLa (cervical cancer), the cell lines attained were as (MCF-7-ATCC®HTB-22™, HCT116-ATCC®CCL-247™, and HeLa-ATCC®CCL-2™, preserved with Dulbecco's Modified Eagle's Medium (DMEM) accompanied with 1% L-glutamine, 10% fetal bovine serum, and 1% penicillin-streptomycin (Gibco) at 37 °C with a humidity of 5 percent CO_2. Cells (trypsinized with Trypsin-EDTA 0.25%, TFS) were rested (5 min) at 5 percent CO_2 humidity before defusing with 1:1 of DMEM and finally placed under 1000× rpm in a centrifuge (5 min). Following three to six treatments, cells were situated in 96-well plates at 10^4 cells/well and maintained in DMEM for 24 h. The cells were independently reacted with β-Nb_2ZnO_6 (**A**) and (**B**) nanoparticles (at concentrations 1, 0.5, 0.25, and 0.125 mg/mL) with a dilution of 1 mL DMEM and 100 mL of each of the above was used in replicates of two post removal of precultured media and incubation period of 24, 48, and 72 h.

The viability check was done two times by addition of MTT solution (Sigma) prepared as 5 mg/mL in 1 × phosphate-buffered saline. MTT (10 μL solution) was placed into each well as well as positive controls with 0.5 mg/mL concentration. The assay was carried out for 4 h at 37 °C at the end of which, 100 μL of dimethyl sulfoxide (DMSO) was introduced to bring about the conversion of tetrazolium salts to formazan by metabolically active cells. Spectra at 570 nm were noted with the help of SYNERGY Neo2 multi-mode microplate reader, Biotek, to compute cell viability as

$$\text{Cell viability (\%)} = \text{Abs}_{\text{sample}}/\text{Abs}_{\text{control}} \times 100$$

MTT cell viability results were stated as the mean ± standard deviation (SD) of two objective experiments. The results were subjected to the ordinary two-way ANOVA test which was carried out by GraphPad Prism Software (GrapPad, La Jolla, CA, USA). In all cases, p-value ≤ 0.05 was considered significant (GP: 0.1234 (ns), 0.332 (*), 0.0021 (**), 0.0002 (***), <0.0001 (****)).

3.4. Imaging by Confocal Microscopy

MCF-7, HCT116, and HeLa cell lines were seeded in 8-well Nunc™ Lab-Tek™ Chamber Slide System (Thermo Fisher Scientific) at 35×10^4 cells/well together with 0.25, 0.5, and 1 mg/mL of each β-Nb_2ZnO_6 (**A**) and (**B**) nanoparticles for 48 h. The cells were fixed using cold absolute methanol for 10 min, then treated with ProLong™ Gold Antifade

Mountant plus DAPI (4′,6-diamidino-2-phenylindole) from TFS. The illustrations were recorded with an LSM 700 confocal microscope (Zeiss, Jena, Germany).

4. Conclusions

β-Nb_2ZnO_6 nanoparticles were effectively designed with nanoplate-like morphology using a hydrothermal method. The sample calcined at 500 °C (**A**) exhibited an improved photocatalytic action for the degradation of methyl orange compared to the sample calcined at 700 °C (**B**). The comprehensive results conclude that sample A is considered more effective on account of enhanced charge carrier separation along with synergistic repressed recombination of electron-hole pairs, making it an ideal photocatalyst. Finally, we examined the cytotoxicity of β-Nb_2ZnO_6 (**A**) and (**B**) nanoparticles at gradual concentrations (1, 0.5, 0.25, and 0.125 mg/mL) against MCF-7, HCT116, and HeLa cells. The results revealed that β-Nb_2ZnO_6 (**A**) and (**B**) nanoparticles exhibited high cytotoxic activity against MCF-7 and HCT116 cells and lower cytotoxic activity towards HeLa cells post 24 and 48 h, which turned to high cytotoxic activity after 72 h. Overall, the EC_{50} values were similar for both (**A**) and (**B**) against each tested cell line with obvious variations between MCF-7 or HCT116 and HeLa cells.

References

1. Chałupniak, A.; Morales-Narváez, E.; Merkoçi, A. Micro and nanomotors in diagnostics. *Adv. Drug Deliv. Rev.* **2015**, *95*, 104–116. [CrossRef] [PubMed]
2. Kerssemakers, J.; Ionov, L.; Queitsch, U.; Luna, S.; Hess, H.; Diez, S. 3D Nanometer Tracking of Motile Microtubules on Reflective Surfaces. *Small* **2009**, *5*, 1732–1737. [CrossRef] [PubMed]
3. Takatsuki, H.; Tanaka, H.; Rice, K.M.; Kolli, M.B.; Nalabotu, S.K.; Kohama, K.; Famouri, P.; Blough, E.R. Transport of single cells using an actin bundle–myosin bionanomotor transport system. *Nanotechnology* **2011**, *22*, 245101. [CrossRef] [PubMed]
4. Saini, V.; Zharov, V.P.; Brazel, C.S.; Nikles, D.E.; Johnson, D.T.; Everts, M. Combination of viral biology and nanotechnology: New applications in nanomedicine. *Nanomed. Nanotechnol. Biol. Med.* **2006**, *2*, 200–206. [CrossRef]
5. Arayne, M.S.; Sultana, N.; Qureshi, F. Review: Nanoparticles in delivery of cardiovascular drugs. *Pak. J. Pharm. Sci.* **2007**, *20*, 340–348. [PubMed]
6. Nawaz, M. Nanotechnology-Based Approaches in Pediatric Parasitic Infections. *J. Pediatr. Infect. Dis.* **2017**, *12*, 264–270. [CrossRef]
7. Khandelwal, H.; Singh, G.; Agrawal, K.; Prakash, S.; Agarwal, R. Characterization of hydroxyapatite coating by pulse laser deposition technique on stainless steel 316 L by varying laser energy. *Appl. Surf. Sci.* **2013**, *265*, 30–35. [CrossRef]
8. Qureshi, F.; Nawaz, M.; Rehman, S.; Almofty, S.A.; Shahzad, S.; Nissapatorn, V.; Taha, M. Synthesis and characterization of cadmium-bismuth microspheres for the catalytic and photocatalytic degradation of organic pollutants, with antibacterial, antioxidant and cytotoxicity assay. *J. Photochem. Photobiol. B Biol.* **2020**, *202*, 111723. [CrossRef]

9.   Shao, H.; Yu, C.; Xu, X.; Ji, W.; Rui, Z.; Xiaojing, W. Influence of TiO$_2$ nanocrystallization on microstructure, interface bonding, surface energy and blood compatibility of surface TiO$_2$ films. *Appl. Surf. Sci.* **2010**, *257*, 1649–1654. [CrossRef]

10.   Wang, M.; Wang, Y.; Chen, Y.; Gu, H. Improving endothelialization on 316L stainless steel through wettability controllable coating by sol–gel technology. *Appl. Surf. Sci.* **2013**, *268*, 73–78. [CrossRef]

11.   Yang, J.; Zhang, J.; Zhu, L.; Chen, S.; Zhang, Y.; Tang, Y.; Zhu, Y.; Li, Y. Synthesis of nano titania particles embedded in mesoporous SBA-15: Characterization and photocatalytic activity. *J. Hazard. Mater.* **2006**, *137*, 952–958. [CrossRef] [PubMed]

12.   Yu, J.C.; Yu, J.; Zhao, J. Enhanced photocatalytic activity of mesoporous and ordinary TiO2 thin films by sulfuric acid treatment. *Appl. Catal. B-Environ.* **2002**, *36*, 31–43. [CrossRef]

13.   Khaleel, A.; Nawaz, M.; Al-Hadrami, S.; Greish, Y.; Saeed, T. The effect of metal ion dopants (V^{3+}, Cr^{3+}, Fe^{3+}, Mn^{2+}, Ce^{3+}) and their concentration on the morphology and the texture of doped γ-alumina. *Microporous Mesoporous Mater.* **2012**, *168*, 7–14. [CrossRef]

14.   Khaleel, A.; Nawaz, M.; Hindawi, B. Sol-gel derived Cr(III) and Cu(II)/γ-Al$_2$O$_3$ doped solids: Effect of the dopant precursor nature on the structural, textural and morphological properties. *Mater. Res. Bull.* **2013**, *48*, 1709–1715. [CrossRef]

15.   Khaleel, A.; Nawaz, M. Enhanced catalytic complete oxidation of 1,2-dichloroethane over mesoporous transition-metal doped gamma-Al$_2$O$_3$. *J. Environ. Sci.* **2015**, *29*, 199–209. [CrossRef]

16.   Khaleel, A.; Nawaz, M. The effect of composition and gel treatment conditions on the textural properties, reducibility and catalytic activity of sol-gel prepared Fe-(III)-Cr(III) bulk mixed oxides. *Colloid Surf. A-Physicochem. Eng. Asp.* **2016**, *488*, 52–57. [CrossRef]

17.   Nawaz, M.; Almofty, S.A.; Qureshi, F. Preparation, formation mechanism, photocatalytic, cytotoxicity and antioxidant activity of sodium niobate nanocubes. *PLoS ONE* **2018**, *13*, e0204061. [CrossRef]

18.   Nawaz, M.; Akhtar, S.; Qureshi, F.; Almofty, S.A.; Nissapatron, V. Preparation of indium-cadmium sulfide nanoparticles with diverse morphologies: Photocatalytic and cytotoxicity study. *J. Mol. Struct.* **2021**, *1253*, 132288. [CrossRef]

19.   Lin, W. Introduction: Nanoparticles in Medicine. *Chem. Rev.* **2015**, *115*, 10407–10409. [CrossRef]

20.   Lu, Y.; Hu, Q.; Lin, Y.; Pacardo, D.B.; Wang, C.; Sun, W.; Ligler, F.S.; Dickey, M.; Gu, Z. Transformable liquid-metal nanomedicine. *Nat. Commun.* **2015**, *6*, 10066. [CrossRef]

21.   Sanvicens, N.; Marco, M.-P. Multifunctional nanoparticles–properties and prospects for their use in human medicine. *Trends Biotechnol.* **2008**, *26*, 425–433. [CrossRef] [PubMed]

22.   Zhang, L.; Gu, F.; Chan, J.; Wang, A.; Langer, R.S.; Farokhzad, O.C. Nanoparticles in Medicine: Therapeutic Applications and Developments. *Clin. Pharmacol. Ther.* **2008**, *83*, 761–769. [CrossRef]

23.   Stanley, S.A.; Sauer, J.; Kane, R.S.; Dordick, J.S.; Friedman, J.M. Remote regulation of glucose homeostasis in mice using genetically encoded nanoparticles. *Nat. Med.* **2015**, *21*, 92–98. [CrossRef] [PubMed]

24.   Mahboob, T.; Nawaz, M.; Tian-Chye, T.; Samudi, C.; Wiart, C.; Nissapatorn, V. Preparation of Poly (dl-Lactide-co-Glycolide) Nanoparticles Encapsulated with Periglaucine A and Betulinic Acid for In Vitro Anti-Acanthamoeba and Cytotoxicity Activities. *Pathogens* **2018**, *7*, 62. [CrossRef] [PubMed]

25.   Wu, C.-Y.; Young, D.; Martel, J.; Young, J.D. A story told by a single nanoparticle in the body fluid: Demonstration of dissolution-repreipitation of nanocrystals in a biological system. *Nanomedicine* **2015**, *10*, 2659–2676. [CrossRef] [PubMed]

26.   Yasur, J.; Rani, P.U. Lepidopteran insect susceptibility to silver nanoparticles and measurement of changes in their growth, development and physiology. *Chemosphere* **2015**, *124*, 92–102. [CrossRef]

27.   Tun, L.; Libo, W.; Ye, J.; Qiuwen, L.; Caijin, H. Hexagonal boron nitride nanoplates as emerging biological nanovectors and their potential applications in biomedicine. *J. Mater. Chem. B* **2016**, *4*, 6103–6110.

28.   Schuemann, J.; Bagley, A.F.; Berbeco, R.; Bromma, K.; Butterworth, K.T.; Byrne, H.L.; Chithrani, B.D.; Cho, S.H.; Cook, J.R.; Favaudon, V.; et al. Roadmap for metal nanoparticles in radiation therapy: Current status, translational challenges, and future directions. *Phys. Med. Biol.* **2020**, *65*, 21RM02. [CrossRef]

29.   Nawaz, M. Morphology-controlled preparation of Bi2S3-ZnS chloroplast-like structures, formation mechanism and photocatalytic activity for hydrogen production. *J. Photochem. Photobiol. A Chem.* **2017**, *332*, 326–330. [CrossRef]

30.   Penninckx, S.; Heuskin, A.-C.; Michiels, C.; Lucas, S. Gold Nanoparticles as a Potent Radiosensitizer: A Transdisciplinary Approach from Physics to Patient. *Cancers* **2020**, *12*, 2021. [CrossRef]

31.   Canaparo, R.; Foglietta, F.; Limongi, T.; Serpe, L. Biomedical Applications of ReactiveOxygen Species Generation by Metal Nanoparticles. *Materials* **2021**, *14*, 53. [CrossRef] [PubMed]

32.   Pradeep PremKumar, K.; Duraipandy, N.; Kiran, M.S.; Rajendrana, N. Antibacterial effects, biocompatibility and electrochemical behavior of zinc incorporated niobium oxide coating on 316L SS for biomedical applications. *Appl. Surf. Sci.* **2018**, *427*, 1166–1181.

33.   Liang, Z.; Yan, C.-F.; Rtimi, S.; Bandara, J. Piezoelectric materials for catalytic/photocatalytic removal of pollutants: Recent advances and outlook. *Appl. Catal. B Environ.* **2019**, *241*, 256–269. [CrossRef]

34.   Chaojun, Z.; Weihua, F.; Haoqing, W.; Najun, L.; Dongyun, C.; Qingfeng, X.; Hua, L.; Jinghui, H.; Jianmei, L. p-n Heterojunction of BiOI/ZnO nanorod arrays for piezo-photocatalytic degradation of bisphenol A in water. *J. Hazard. Mater.* **2020**, *399*, 123109.

35.   Xiaoyi, S.; Youjiang, S.; Hongmei, S.; Yan, L.; Yuchun, Z. Synthesis and photocatalytic degradation ability evaluation for rhodamine B of ZnO@SiO$_2$ composite with flower-like structure. *Water Sci. Technol.* **2020**, *80*, 1986–1995.

36.   Zhen, L.; Dan, J.; Zhenghua, W. ZnO/CdSe-diethylenetriamine nanocomposite as astep-scheme photocatalyst for photocatalytic hydrogen evolution. *Appl. Surf. Sci.* **2020**, *529*, 147071.

37. Bingxuan, N.; Dapeng, W.; Jinshui, W.; Le, W.; Wenlong, Z. Salt-sealing-pyrolysis derived Ag/ZnO@C hollow structures towards efficient photo-oxidation of organic dye and water-born bacteria. *Appl. Surf. Sci.* **2020**, *528*, 146965.

38. Yan, Y.; Binghua, Y.; Yangqing, H.; Baoyue, C.; Youliang, R.; Qiangqiang, S. Piezo-enhanced photodegradation of organic pollutants on Ag_3PO_4/ZnO nanowires using visible light and ultrasonic. *Appl. Surf. Sci.* **2020**, *528*, 146819.

39. Nawaz, M.; Fangzhi, M.; Leilei, X.; Hao, T.; Jianguo, G. F–Bi_4TaO_8Cl flower-like hierarchical structures: Controlled preparation, formation mechanism and visible photocatalytic hydrogen production. *RSC Adv.* **2017**, *7*, 121–127. [CrossRef]

40. Nawaz, M.; Fangzhi, M.; Leilei, X.; Jianguo, G. Effect of solvents and reaction parameters on the morphology of Ta_2O_5 and photocatalytic activity. *J. Mol. Liq.* **2018**, *269*, 211–216. [CrossRef]

41. Soci, C.; Zhang, A.; Xiang, B.; Dayeh, S.A.; Aplin, D.P.R.; Park, J.; Bao, X.Y.; Lo, Y.H.; Wang, D. ZnO Nanowire UV Photodetectors with High Internal Gain. *Nano Lett.* **2007**, *7*, 1003–1009. [CrossRef] [PubMed]

42. Wang, P.; Huang, B.; Zhang, X.; Qin, X.; Dai, Y.; Jin, H.; Wei, J.; Whangbo, M.-H. Composite Semiconductor $H_2WO_4 \cdot H_2O$/AgCl as an Efficient and Stable Photocatalyst under Visible Light. *Chem. Eur. J.* **2008**, *14*, 10543–10546. [CrossRef] [PubMed]

43. Xia, D.; An, T.; Li, G.; Wang, W.; Zhao, H.; Wong, P.K. Synergistic photocatalytic inactivation mechanisms of bacteria by graphene sheets grafted plasmonic AgAgX (X = Cl, Br, I) composite photocatalyst under visible light irradiation. *Water Res.* **2016**, *99*, 149–161. [CrossRef] [PubMed]